Energies **2014**, *7*, 1393-1426; doi:10.3390/en7031393

OPEN ACCESS

energies

ISSN 1996-1073

www.mdpi.com/journal/energies

Article

Investigation of the Cooling and Thermal-Measuring System of a Compound-Structure Permanent-Magnet Synchronous Machine

Jingang Bai, Yong Liu *, Yi Sui, Chengde Tong, Quanbin Zhao and Jiawei Zhang

Department of Electrical Engineering, Harbin Institute of Technology, Harbin 150080, Heilongjiang, China; E-Mails: baijingangdiyi@163.com (J.B.); suiyi_hitee2005@163.com (Y.S.); tongchengde@126.com (C.T.); binqzhao@gmail.com (Q.Z.); zjwhit09@163.com (J.Z.)

* Author to whom correspondence should be addressed; E-Mail: yliu@hit.edu.cn; Tel./Fax: +86-451-8641-3623.

Received: 17 October 2013; in revised form: 18 February 2014 / Accepted: 19 February 2014 / Published: 7 March 2014

Abstract: The compound-structure permanent-magnet synchronous machine (CS-PMSM) is a power-split device which can enable the internal combustion engine (ICE) to operate at optimum efficiency during all driving conditions by controlling its torque and speed. However, the CS-PMSM has more serious temperature rise and heat dissipation problems than conventional permanent-magnet (PM) machines, especially when the CS-PMSM is running at low speed and under full load conditions. As the thermal resistance of double-layer air gaps is quite big, the hot spot proves to be in the inner winding rotor. To ensure the safe operation of the CS-PMSM, the use of forced-air and water cooling in the inner winding rotor are investigated. The study shows that the water cooling can provide a better cooling effect, but require a complicated mechanical structure. Considering the complexity of the high efficiency cooling system, a real-time temperature monitoring method is proposed and a temperature measuring system which can accurately measure the real-time temperature of multiple key points in the machine is developed to promptly adjust the operating and cooling conditions based on the measured temperature results. Finally, the temperature rise experiment of the CS-PMSM prototype is done and the simulation results are partly validated by the experimental data.

Keywords: compound-structure permanent-magnet synchronous machine (CS-PMSM); cooling system; heat dissipation; real-time; thermal-field; temperature monitoring; temperature rise

1. Introduction

The Toyota Prius has drawn increasingly wide attention from a great many automobile manufacturers and consumers in recent years, owing to its low energy consumption and excellent vehicle performance [1–5]. This mainly benefits from the utilization of a planetary gear unit for power splitting in the Prius hybrid system [6–8]. The planetary gear unit with two machines enables the internal combustion engine (ICE) to operate at optimum efficiency during all driving conditions by controlling its torque and speed [2,6–9], yet adds additional mechanical complexity and maintenance issues [10–12]. To get rid of the planetary gear unit, a compound-structure permanent-magnet synchronous machine (CS-PMSM) is proposed [13,14]. The CS-PMSM, also known as four-quadrant transducer (4QT) [15], electrical variable transmission [16] or dual mechanical port (DMP) machine [17], comprises a stator machine (SM) and a double-rotor machine (DRM) [15], as shown in Figure 1. The inner winding rotor and the outer rotor are mechanically connected with the ICE and the reduction gear, respectively. The DRM transfers the torque from ICE to the reduction gear, and provides the speed difference between the ICE and the reduction gear; and the SM provides torque difference between the ICE and the reduction gear according to the requirements of vehicle load. Therefore, the CS-PMSM can realize the same function of the planetary gear unit, generator and motor in the Prius hybrid system [18–20].

Figure 1. Schematic diagram of the compound-structure permanent-magnet synchronous machine (CS-PMSM) hybrid system. ICE: internal combustion engine.

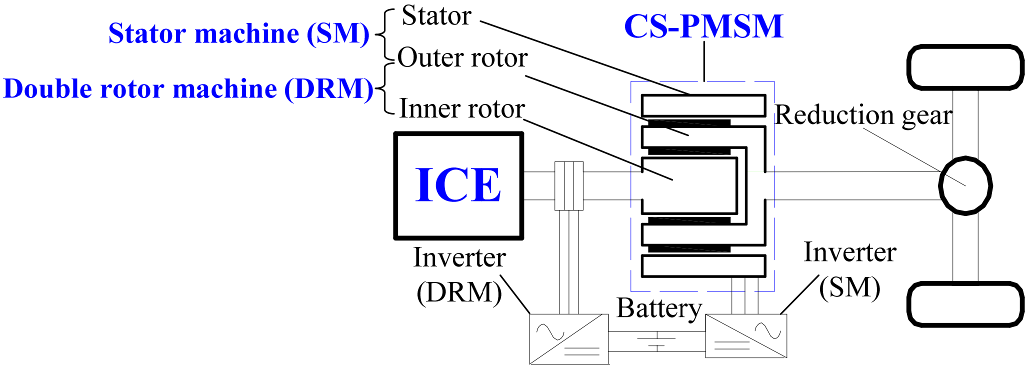

The typical operating modes of the CS-PMSM under hybrid electric vehicle (HEV) operation conditions are analyzed [21]. The control strategies and energy management strategies of the CS-PMSM system are proposed [22,23]. In the design, an electromagnetic-thermal-mechanical design method is proposed [24]. The magnetic coupling and mechanical coupling models are investigated [25–31]. Meanwhile, the performance of CS-PMSM and HEV working condition experiments are tested [32–34]. To solve the magnetic coupling problem in the CS-PMSM, a magnetic decoupling design method is proposed [35–37]. In [38], the inductance parameters considering the cross coupling effect were calculated. Reference [39] proved that the copper loss is dramatically increased for the inner rotor windings owing to the deep slot structure used for the inner rotor and the eddy current effect. In [40], the authors analyzed the heat-dissipating conditions and the manufacturing technology of six CS-PMSM topologies. In [41,42], the thermal field distribution of the CS-PMSM and the cooling effect of the cooling system were analyzed by two-dimensional (2-D) finite-element method (FEM) simulation, although these simulations only focused on the CS-PMSM rated operation.

This paper mainly focuses on the two worst operating conditions, *i.e.*, the rated speed and full load conditions and the low speed and full load conditions. Meanwhile, the cooling effects of the forced-air cooling and water cooling have been investigated comparatively. This can provide a theoretical basis for the design of the cooling system. In order to analyze the axial thermal field distribution, three-dimensional (3-D) FEM is used in this paper. For the random winding machine, it is quite difficult to accurately model the end windings; therefore, a coupling surface method is proposed to simplify 3-D thermal model of the end windings. More importantly, this method can compute the heat transfer effect in the end windings as well as that between end windings and the windings in the slots. To monitoring the temperature of the CS-PMSM, a real-time multi-point temperature measuring system is built. In order to eliminate the error caused by the lead wire and component precision of the circuit and to suppress the electromagnetic interference (EMI) produced by the operating machine, the linear calibration and the four-term Blackman-Harris windowed average method are employed in this system.

2. Structure of the CS-PMSM

The schematic diagram of this CS-PMSM prototype is shown in Figure 2. The main parameters of this machine are listed in Table 1.

Figure 2. Schematic diagram of the cooling system of the CS-PMSM prototype.

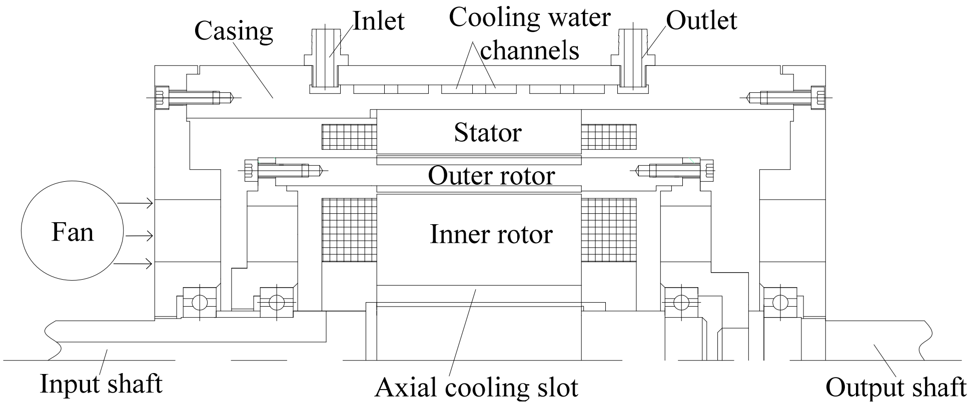

Table 1. Main parameters of the CS-PMSM.

Parameters	Value	Parameters	Value
Rated power of SM (kW)	10	Stator core internal diameter (mm)	192.6
Rated power of DRM (kW)	10	Outer rotor external diameter (mm)	190.6
Rated current of SM (A)	32	Outer rotor internal diameter (mm)	157
Rated current of SM (A)	32	Inner rotor external diameter (mm)	155
Casing external diameter (mm)	275	Inner rotor internal diameter (mm)	50
Stator core external diameter (mm)	234	Axial length of core lamination (mm)	95

As can be seen from Figure 2, the casing is double-layer, and the cooling water channels are manufactured between the two layers of the casing. The cooling water channels are eight circular channels with tops or bottoms connected, and both the inlet and the outlet of channels are distributed at the top of the casing.

Figure 3 is a schematic diagram of the water flow in the water channels. It indicates that the water cooling system is symmetrical about the longitudinal section including the inlet and outlet.

Figure 3. Schematic diagram of the water flow in the water channels.

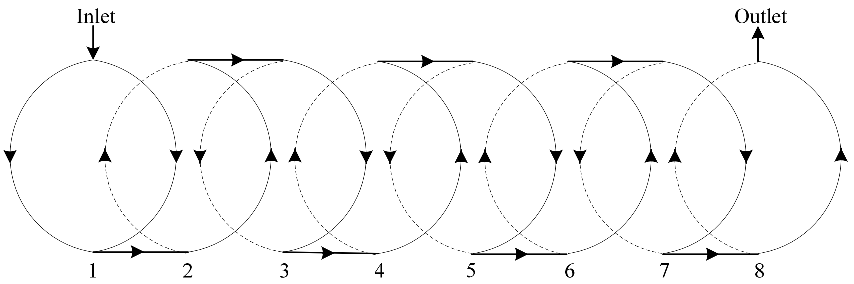

In the inner rotor, there are six axial cooling slots along circumferential direction, as shown in Figure 4. They can provide a cooling wind path. On one machine side, an external fan is used to provide the force air.

Figure 4. Schematic diagram of axial cooling slots.

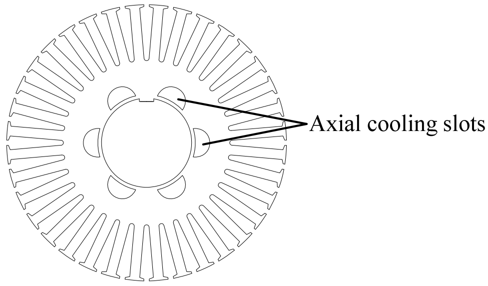

From the above illustration of the cooling system and mechanical structure of the CS-PMSM prototype, we know that when the cooling water with a certain pressure flows through the cooling water channels of the casing, there must be a temperature difference generated in both the axial and circumferential directions of the CS-PMSM. Besides, a temperature difference along the axial direction also exists when one side of the machine is cooled by the fan. Therefore, the thermal field analysis of the CS-PMSM prototype is a typical 3-D problem. However, 3-D thermal field analysis is much more complicated than 2-D thermal field analysis. In the machine, the high-temperature spots usually happen in the core or the windings; therefore, the 3-D model doesn't contain the end cover and bearing closure. The influence of the end cover and bearing enclosure on the thermal field in this machine is taken into account by selecting a suitable heat transfer coefficient for the end windings and end regions. The 3-D model contains the effective parts of CS-PMSM, end windings of stator and inner rotor, and the cooling system, which are described in the following text.

3. Thermal-Field Analysis Model of the CS-PMSM

3.1. Losses of the CS-PMSM

The copper losses are computed from the currents and the measured resistances, which can be expressed as:

$$P_{\mathrm{Cu}} = 3I_{\mathrm{ph}}{}^2R_{\mathrm{ph}} \tag{1}$$

where P_{Cu} is the copper loss; R_{ph} is the per-phase measured resistance; and I_{ph} is the per-phase current.

The core loss in the steel lamination regions are computed by:

$$P_{\mathrm{c}} = K_{\mathrm{e}}f^2B_{\max}^2 + K_{\mathrm{h}}fB_{\max}^a \tag{2}$$

where P_{c} is the core loss; f is the magnetic field frequency; $B_{\max}$ is the magnetic field amplitude; K_{e} is the eddy current loss coefficient; K_{h} is the hysteresis loss coefficient; and a is the coefficient determined by the magnetic field waveform and amplitude. K_{e}, K_{h} and a can be obtained from the loss curve *versus* the magnetic field [43].

The Eddy current loss in PMs is computed by:

$$P_{\mathrm{pm}} = \frac{1}{T}\int_0^T\int_V \frac{J_{\mathrm{e}}^2}{\sigma}dvdt \tag{3}$$

where J_{e} is eddy current density in PMs; and σ is the PM conductivity.

Under the rated load condition, the electrical loading, magnetic loading, current density in the slots are listed in Table 2.

Table 2. Main parameters under CS-PMSM rated load condition.

Parameters	Value	Parameters	Value
Electrical loading of SM (A/m)	1.523×10^4	Electrical loading of DRM (A/m)	2.129×10^4
Magnetic loading of SM (T)	0.7	Magnetic loading of DRM (T)	0.78
Current density in SM slots (A/m^2)	5.42×10^6	Current density in DRM slots (A/m^2)	5.42×10^6

The flux density of the CS-PMSM is shown in Figure 5.

Figure 5. Flux density distribution under rated load condition.

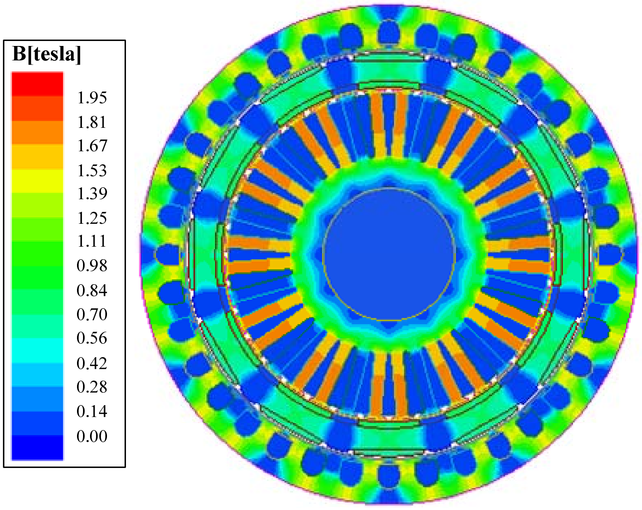

With the material property changing with temperature considered, the copper resistance and the magnet B/H curve are obtained under a pre-specified temperature, and then they are modified according to the thermal-filed results. Eventually, the losses listed in this paper are the results of the electromagnetic-thermal bi-directional accordance, as shown in Table 3.

Table 3. Losses on rated load condition.

Position	Loss (W)	Position	Loss (W)
Straight part of stator windings	92.1	Inner permanent magnets	82.6
Stator end windings	142.3	Straight part of inner rotor windings	121.7
Stator teeth	170.4	Inner rotor end windings	97
Stator yoke	117.1	Inner rotor teeth	423.4
Outer permanent magnets	58.6	Inner rotor yoke	183.8
Outer rotor core	14.5	-	-

3.2. Equivalent Processing of the Thermal Field Model

In this paper, the finite-element analysis (FEA) simulation mainly focuses on the steady-state thermal field analysis under the SM and DRM rated load conditions. According to the previous analysis about the cooling system of the CS-PMSM prototype, it is clear that there are mainly water-cooling, forced-air and natural convective heat transfer and conduction heat transfer in the CS-PMSM. Although radiation heat transfer is always happening, especially when the rotor speed is very low or zero [44], radiation heat transfer is normally neglected when the forced convection is mainly responsible of the motor cooling [45,46]. Hence the following assumptions in the FEA calculation are given by:

(1) Only the convective and conduction heat transfer are considered;
(2) The heat sources are uniformly distributed on the corresponding regions of the CS-PMSM.

According to the symmetrical characteristic of the CS-PMSM structure and cooling system in circumferential direction, a 3-D FEA model with half of the CS-PMSM is built to analyze the thermal field, as shown in Figure 6.

Figure 6. Three-dimensional (3-D) finite-element analysis (FEA) model of the CS-PMSM thermal field.

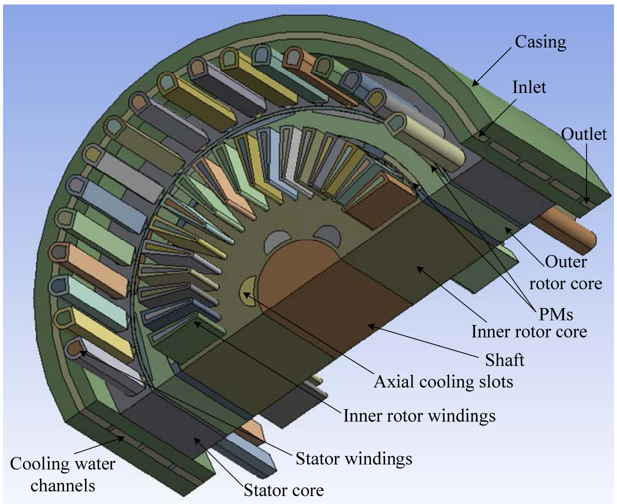

The 3-D FEA model of the cooling water channel in the stator is shown in Figure 7. In the machine, modeling of the windings and air gap is very important for the thermal field analysis. Hence the model of the windings and air gap will be illustrated in the following text.

Figure 7. 3-D FEA model of the cooling water channel.

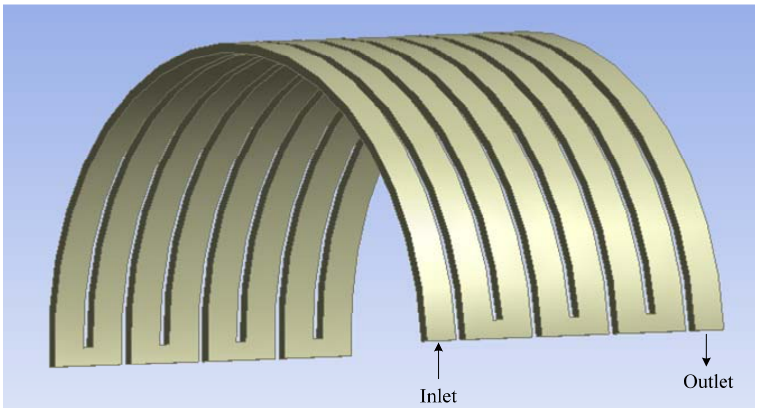

In 3-D modeling process of the CS-PMSM, to build an accurate model of the windings is quite difficult. This is mainly because the conductors in each coil are randomly distributed inside the slots. The random distribution of the conductors in the slots has a certain influence on the maximum temperature of the windings [47]. Besides, the insulation layer of the conductor is thin, which will bring us a big problem in the model meshing. An effective equivalent method of the distributed conductors is normally used in the 2-D thermal field analysis [48], as shown in Figure 8.

Figure 8. Equivalent process of the windings.

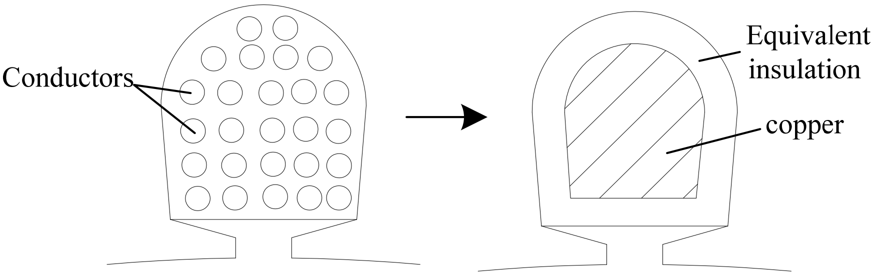

An equivalent copper conductor, whose area equals the sum of all copper conductor areas, is put in the center of the slot. And an equivalent insulation, which consists of the slot insulation, the equivalent air gap layer and the equivalent insulation varnish layer, is evenly put outside the equivalent copper conductor. On the basis of this method, the 3-D winding models in the slots, considering both radial and axial heat transfer effect, are built in this paper.

In Figure 8, the thermal conductivity of the equivalent insulation λ_{eq} is given by:

$$\lambda_{\mathrm{eq}} = \frac{d_1 + d_2 + d_3}{\dfrac{d_1}{\lambda_1} + \dfrac{d_2}{\lambda_2} + \dfrac{d_3}{\lambda_3}} \tag{4}$$

where d_1 is the thickness of the slot insulation; d_2 is the thickness of the air gap layer; d_3 is the thickness of the equivalent insulation varnish layer; and λ_1, λ_2, λ_3 are the corresponding thermal conductivities.

In the CS-PMSM, these parameters have the following values for the stator windings: $d_1 = 0.3$ mm, $d_2 = 0.7$ mm, $d_3 = 0.6$ mm, $\lambda_1 = 0.15$ W/m·K, $\lambda_2 = 0.0242$ W/m·K, $\lambda_3 = 0.35$ W/m·K. Therefore, the thickness of the equivalent insulation is 1.6 mm and its equivalent thermal conductivity is 0.049 W/m·K for the stator windings. In the inner rotor windings, the parameters are listed as follows: $d_1 = 0.3$ mm,

d_2 = 0.7 mm, d_3 = 0.4 mm, λ_1 = 0.15 W/m·K, λ_2 = 0.0242 W/m·K, λ_3 = 0.35 W/m·K. Therefore, the thickness of the equivalent insulation is 1.4 mm and its equivalent thermal conductivity is 0.044 W/m·K for the inner rotor windings. Although the above equivalent method is a method to analyze the radial heat transfer effect, the extrusion 3-D model of the above equivalent model can also analyze the axial heat transfer effect. The 3-D models of the stator and inner rotor windings are shown in Figure 9.

Figure 9. (**a**) Stator winding equivalent model; and (**b**) inner rotor winding equivalent model.

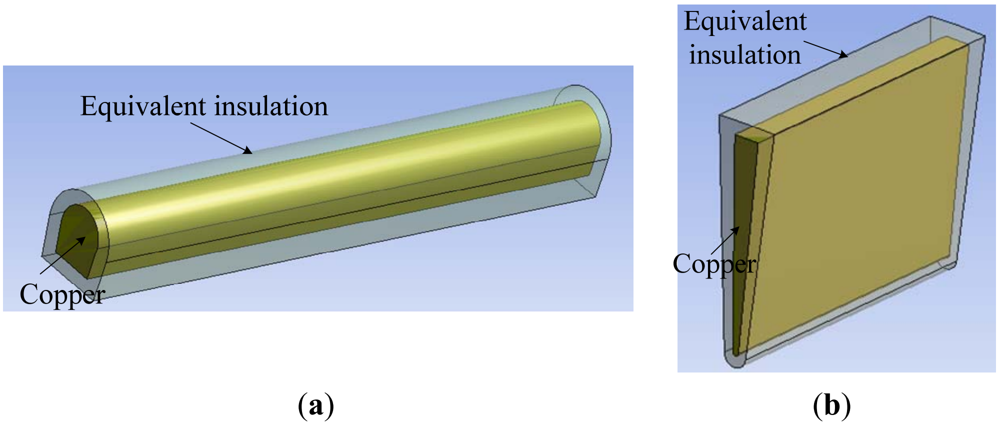

To build an accurate model of the end windings is more difficult than the winding model in the slot. This is mainly because the shape of each end winding isn't exactly the same and is also difficult to ascertain for the distributed-conductor machine. Therefore, this paper presents a simplified model of the end windings, as shown in Figure 10. Each end winding is equivalent to the two linear-structure windings. The axial length sum of the two linear-structure windings equals the length of one end winding. The linear-structure winding model and its equivalent parameters are the same as that in the slot. To simulate the heat transfer effect in the actual end winding, the end surfaces of two linear-structure windings are set to coupling surfaces to ensure the heat transfer between the two linear-structure windings. Therefore, the heat dissipation of linear-structure end windings depends on their surface (S_1 and S_2) heat convection coefficient and ambient temperature.

Figure 10. (**a**) Stator end winding simplified model; and (**b**) inner end winding simplified model.

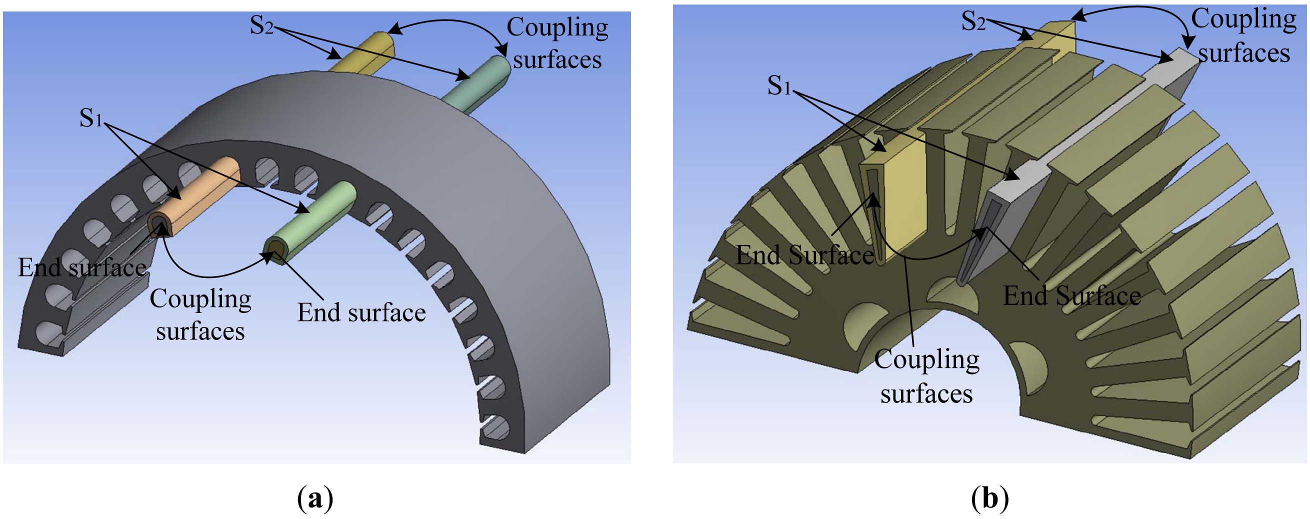

When both the SM and the DRM are operating, there is a relative rotation between the stator and outer rotor as well as between the outer rotor and the inner rotor, so it makes the air in the inner and outer air gap flow relatively, which brings about convective heat transfer between the air gap and neighbor parts. In order to simplify the calculation, the flowing air in the inner and outer air gap is equivalent as a still air with an equivalent heat conductivity coefficient. Before the calculation of equivalent heat conductivity coefficient, the following definition for the generic hollow-cylindrical air gap is first given by:

$$\eta = \frac{R_o}{R_i} \tag{5}$$

$$Re = \frac{\omega\delta}{v} \tag{6}$$

where R_i is the inner radius of the air gap (m); R_o is the outer radius of the air gap (m); ω is the peripheral speed of the inner rotation component (m/s); δ is the air gap length (m); v is the kinematic viscosity of air (m^2/s). Then the equivalent heat conductivity coefficient [48–50] can be calculated as:

$$\lambda_{eff} = 0.0019 \cdot \eta^{-2.9084} \cdot Re^{0.4614\ln(3.33361\cdot\eta)} \tag{7}$$

When the SM and the DRM are operating under their rated speed condition, the speeds of the inner and outer rotor are 6000 rpm and 3000 rpm, respectively. In the CS-PMSM, the speed of the DRM is the speed difference between the inner and outer rotor. Therefore, the rated speed of the DRM is 3000 rpm. The corresponding parameters have the following values for the inner air gap: $R_i = 77.5 \times 10^{-3}$ m, $R_o = 78.5 \times 10^{-3}$ m, $\omega = 24.3$ m/s, $\delta = 1 \times 10^{-3}$ m, and $v = 14.8 \times 10^{-6}$ m^2/s. For the outer air gap, the parameters are listed as follows: $R_i = 95.3 \times 10^{-3}$ m, $R_o = 96.3 \times 10^{-3}$ m, $\omega = 29.9$ m/s, $\delta = 1 \times 10^{-3}$ m, and $v = 14.8 \times 10^{-6}$ m^2/s. According to the Equation (3), the equivalent heat conductivity coefficient is 0.116 W/m·K for the inner air gap and 0.13 W/m·K for the outer air gap, respectively.

During the machine manufacturing process, a binding band with thickness of 0.8 mm is used to fix the outer-layer permanent magnets. Considering the thin structure of the binding band, the mesh generated in the binding band component will be very small, which takes a lot of calculation time, therefore, further equivalent processing is carried out on the outer air gap and the binding band. The thermal conductivity of the equivalent outer air gap λ_{eq_o} is given by:

$$\lambda_{eq\_o} = \frac{\delta_o + d_b}{\frac{\delta_o}{\lambda_o} + \frac{d_b}{\lambda_b}} \tag{8}$$

where δ_o and d_b are the thickness of the outer air gap and the binding band respectively; λ_o and λ_b are the corresponding thermal conductivities. In the calculation, the corresponding parameters are listed as follows: $\delta_o = 1$ mm, $d_b = 0.8$ mm, $\lambda_o = 0.13$ W/m·K, and $\lambda_b = 0.22$ W/m·K. Finally the equivalent heat conductivity coefficient of the outer air gap is 0.159 W/m·K.

3.3. Boundary and Thermal Parameters Calculation

In the cooling water channels of the stator, the fluid-thermal field can be calculated by the given inlet and outlet boundary conditions. The velocity-inlet and pressure-outlet boundaries are imposed on the inlet and outlet of the cooling water channels, respectively. The flow velocity of the cooling water and the water temperature on the inlet are 0.7 m/s and 21 °C, respectively, which is consistent with the test condition. The measured water temperature on the outlet is 25 °C, which is used as the temperature condition of the pressure-outlet boundary.

For the heat convection of the outer surface of the casing and the end windings, the Robin boundary condition is given as:

$$\lambda \nabla T \cdot \vec{n} + \alpha (T - T_{\mathrm{f}}) = 0 \tag{9}$$

where T and λ are the temperature (in degrees Celsius) and the thermal conductivity of the corresponding region (in W/m·K); $\vec{n}$ is the unit normal vector on the surface; α is the heat transfer coefficient (in $\mathrm{W/m^2 \cdot K}$); and T_{f} is the ambient temperature (in degrees Celsius). In the calculation, α and T_{f} are only needed to be specified.

For the outer surface of the casing, its measured ambient temperature is 21 °C and its heat transfer coefficient is determined by:

$$\alpha = 9.73 + 14 v_{\mathrm{c}}^{0.62} \tag{10}$$

where v_{c} is the airflow speed on the surface of the casing [50]. As the outer surface of the casing has no airflow, 9.73 $\mathrm{W/m^2 \cdot K}$ is adopted as the heat transfer coefficient of outer surface.

For the outer surface of the end windings, the equivalent heat transfer coefficient is determined by:

$$\alpha = 41.4 + 6.22 v_{\mathrm{e}} \tag{11}$$

where v_{e} is the airflow speed in end winding space [45,46]. The wind speeds on the windward and leeward sides of the end winding space are 36 m/s and 5.5 m/s, respectively, so the heat transfer coefficients are 265.3 $\mathrm{W/m^2 \cdot K}$ for the windward side and 75.6 $\mathrm{W/m^2 \cdot K}$ for the leeward side, respectively. The ambient temperatures of the windward and leeward sides for the end windings are 34 °C and 51 °C under the rated speed and full load condition. The ambient temperatures of the windward and leeward sides for the end windings are 34 °C and 37 °C under the low speed and full load condition.

According to the calculated losses of different parts under the CS-PMSM rated load condition, the heating rates of corresponding parts are obtained, as shown in Table 4.

Table 4. Heating rates of different parts of the machine under rated load.

Position	**Heating rate ($\mathrm{W/m^3}$)**	**Position**	**Heating rate ($\mathrm{W/m^3}$)**
Straight part of Stator windings	5.61×10^5	Inner permanent magnets	8.29×10^5
Stator end windings	5.61×10^5	Straight part of inner rotor windings	6.83×10^5
Stator teeth	3.85×10^5	Inner rotor end windings	6.83×10^5
Stator yoke	2.63×10^5	Inner rotor teeth	7.04×10^5
Outer permanent magnets	5.68×10^5	Inner rotor yoke	4.89×10^5
Outer rotor core	2.77×10^4	-	-

The thermal parameters of machine materials are shown in Table 5.

Table 5. Thermal parameters of the machine materials and cooling fluids.

Position	Materials	Density (kg/m^3)	Specific heat capacity (J/kg·K)	Thermal coefficient (W/m·K)
Casing	45#	7850	480	50.2
Stator core	DW 310-35	7980	450	42.5
Stator winding copper	Copper	8900	407	387
Stator winding equivalent insulation	-	-	-	0.049
PMs	N30UH	7500	504	9
Outer rotor core	20#	7880	480	48
Inner rotor core	DW 310-35	7980	450	42.5
Inner rotor winding copper	Copper	8900	407	387
Inner rotor winding equivalent insulation	-	-	-	0.044
Shaft	45#	7850	480	50.2

4. Thermal Field Analysis under Rated Speed and Rated Load Condition

This paper mainly analyzes the thermal field distribution of two conditions: the rated speed and rated load condition; the low speed and rated load condition. Besides, the thermal field analysis of the two conditions above is based on the actual structure and cooling system of the CS-PMSM prototype.

When both the SM and the DRM are operating under their rated speed and load conditions, both machines output 32 Nm with a speed of 3000 rpm. It is noted that the speed of the DRM is the speed difference between the inner and outer rotor. Since the whole heat productivity is the biggest in this case, there is a serious overheating problem for the CS-PMSM.

When the vehicle is working in the low speed climbing state, both the ICE and the SM are needed to afford the vehicle load torque. In this case, the speed of the SM and the DRM is low, *i.e.*, the relative speed between the stator and the outer rotor as well as that between the outer and inner rotor is extremely low. The air in the inner and outer air gap is almost in a stationary state and its thermal conductivity reduces to 0.0242 W/m·K, so the thermal resistance of the inner and outer air gap is quite big, making the heat-dissipating capability of the inner rotor poor. Therefore, when the SM and the DRM are still running at full load of 32 Nm under the low speed condition, there is still an overheating problem for the CS-PMSM.

4.1. Only Water Cooling Used in the Casing

When both the SM and the DRM are running at the rated speed and rated load, the 3-D thermal field distribution is calculated under condition of only water cooling used in the casing, as shown in Figure 11.

To illustrate the axial thermal field distribution of the CS-PMSM, the thermal field distributions of the water inlet side, middle cross-section, and the water outlet side of the CS-PMSM are shown in Figure 12. In order to eliminate the effects of end face boundary conditions, the selected water inlet and water outlet cross-sections are 2.5 mm away from the corresponding end face, respectively. The highest temperature of different parts in the above three cross-sections is shown in Table 6. Meanwhile, the temperatures of the end windings of the stator and inner rotor are also listed in Table 6.

Figure 11. Thermal field distribution under condition of only water cooling used in the casing when both the SM and the DRM are running at the rated speed and load.

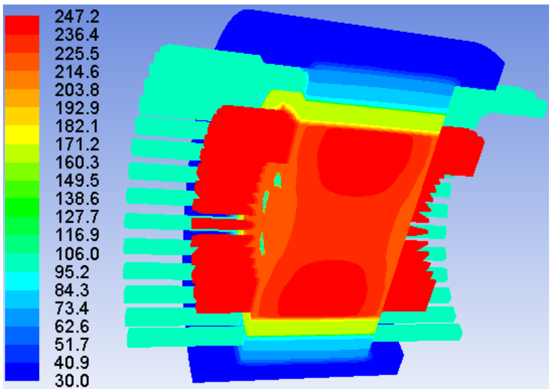

Figure 12. Thermal field distribution of three different cross-sections: (**a**) the water inlet side; (**b**) the middle cross-section; and (**c**) the water outlet side.

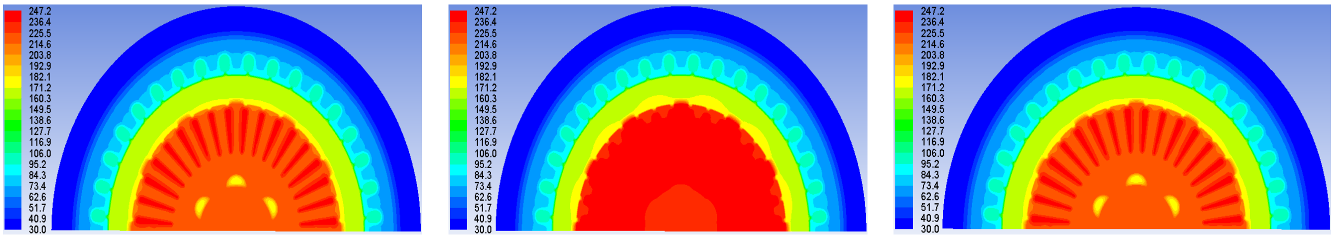

(**a**) (**b**) (**c**)

Table 6. Highest temperatures of different parts in the CS-PMSM.

Regions	**Highest temperature (°C)**		
	Water inlet side	**Middle**	**Water outlet side**
Inner rotor end windings	241.4	-	241.4
Inner rotor windings in the inner rotor core	242.7	247.2	243.9
Inner rotor core	224.1	247	226.8
Inner PMs	172.8	173.9	173
Outer rotor core	170.8	171.6	171.1
Outer PMs	169.8	170.6	170.3
Stator core	88.1	88.4	89.2
Stator windings in the stator core	102	101.2	102.4
Stator end windings	103.6	-	104.7

From the temperature distribution of each cross-section in Table 6, it can be seen that the stator temperature is much lower than the temperature of the inner rotor, indicating that the water cooling used in the casing has a good cooling effect on the stator, but it has a poor cooling effect on the inner rotor. Besides, the temperature of inner rotor has reached 247.2 °C, obviously much higher than the temperature limitation of the class F insulation. By comparison of the temperature of the same part in three cross-sections, it shows that there is a small axial temperature difference for each part within the core length. Since the heat dissipation capacity of stator end windings are poorer than that of the windings in the core, the temperature of the stator end windings is higher than that of the windings in the core. However, the heat dissipation capacity of inner rotor windings in the core is poor for the inner rotor windings, so the temperature of inner rotor windings in the core is higher than that of end windings.

4.2. Water Cooling Used in the Casing and Axial Forced Air

When both the SM and the DRM are running at the rated speed and rated load, the 3-D thermal field distribution is calculated under condition of water cooling used in the casing and axial forced air, as shown in Figure 13.

Figure 13. Thermal field distribution under condition of water cooling used in the casing and axial forced air when both the SM and the DRM are running at the rated speed and rated load.

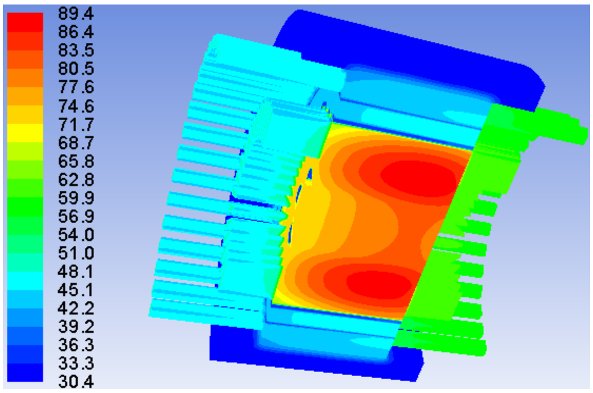

To illustrate the axial thermal field distribution of the CS-PMSM, the thermal field distributions of the windward side, middle cross-section, and the leeward side of the CS-PMSM are shown in Figure 14.

Figure 14. Thermal field distribution of three cross-sections: (**a**) the windward side; (**b**) the middle cross-section; and (**c**) the leeward side.

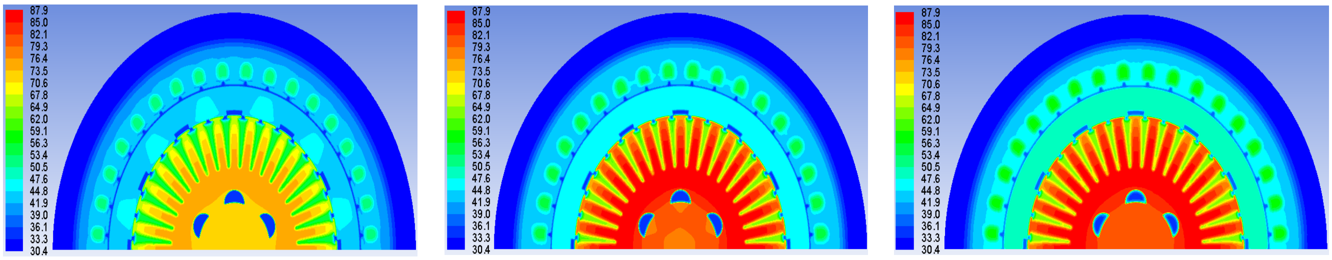

(**a**) (**b**) (**c**)

In order to eliminate the effects of end face boundary conditions, the selected windward and leeward cross-sections are 2.5 mm away from the corresponding end face, respectively. The highest temperature of different parts in the above three cross-sections is shown in Table 7. Meanwhile, the temperatures of the end windings of the stator and inner rotor are also listed in Table 7.

Table 7. Highest temperatures of different parts in the CS-PMSM.

Regions	**Highest temperature (°C)**		
	Windward side	**Middle**	**Leeward side**
Inner rotor end windings	50.1	-	64.8
Inner rotor windings in the inner rotor core	54.7	63.1	64.4
Inner rotor core	74.6	86.8	86.8
Inner PMs	44.8	47.3	48.8
Outer rotor core	44.8	47.1	48.6
Outer PMs	44.7	46.7	48.4
Stator core	43	45	46.1
Stator windings in the stator core	50.9	54	56.7
Stator end windings	48.3	-	58.9

From the temperature distribution of each cross-section in Table 7, it can be seen that the temperatures of the stator and inner rotor are very low, indicating that the axial force air have a good cooling effect on the CS-PMSM, especially for the inner rotor. Meanwhile, due to the existence of axial forced air, there is a certain axial temperature difference for each part within the core length; the temperature of the end windings at windward side is much lower than that at leeward side. By comparison of Tables 6 and 7, it shows that the CS-PMSM can run safely when the water cooling used in the casing and axial forced air are simultaneously adopted in the CS-PMSM.

4.3. Water Cooling Used in the Casing and the Inner Rotor

When both the SM and the DRM are running at the rated speed and rated load, the 3-D thermal field distribution is calculated under condition of water cooling used in the casing and the inner rotor, as shown in Figure 15.

Figure 15. Thermal field distribution under condition of water cooling used in the casing and the inner rotor when both the SM and the DRM are running at the rated speed and rated load.

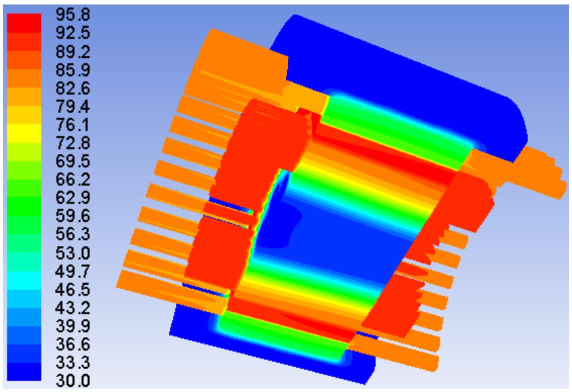

To illustrate the axial thermal field distribution of the CS-PMSM, the thermal field distributions of the water inlet side, middle cross-section, and the water outlet side of the CS-PMSM are shown in Figure 16. The selected water inlet, middle and water outlet cross-sections are the same as those in Section 4.1.

Figure 16. Thermal field distribution of three cross-sections: (**a**) the water inlet side; (**b**) the middle cross-section; and (**c**) the water outlet side.

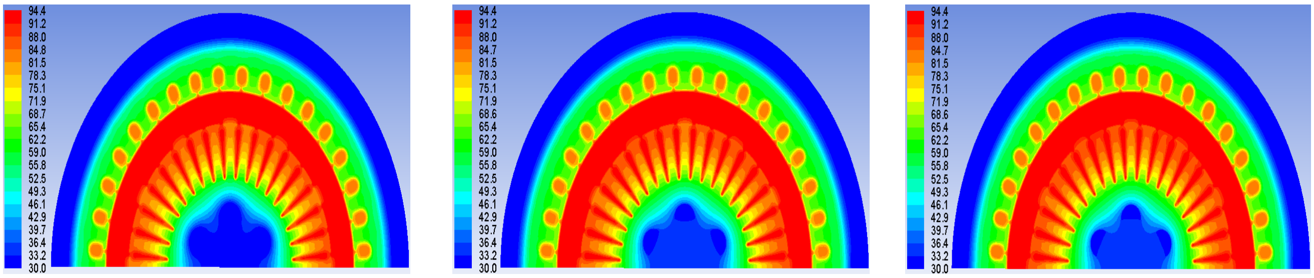

(**a**) (**b**) (**c**)

The highest temperature of each part in the above three cross-sections is shown in Table 8. Meanwhile, the temperatures of the end windings of the stator and inner rotor are also listed in Table 8.

Table 8. Highest temperature of each part in the CS-PMSM.

Regions	Highest temperature (°C)		
	Water inlet side	Middle	Water outlet side
Inner rotor end windings	95.3	-	95.8
Inner rotor windings in the inner rotor core	93.2	93.7	93.9
Inner rotor core	86.9	87.5	88.1
Inner PMs	93.5	93.5	93.7
Outer rotor core	93.2	93.3	93.4
Outer PMs	92.9	93.1	93.2
Stator core	65.7	66.4	66.5
Stator windings in the stator core	83.5	82.7	83.7
Stator end windings	84.7	-	85.8

From the temperature distribution of each cross-section in Table 8, it can be seen that the temperatures of the stator and inner rotor are lower than that of the outer rotor, as the heat of the stator and inner rotor is easily taken away by the water when the water cooling is used in the casing and the inner rotor. By comparison of the temperature of the same part in three cross-sections, it shows that there is a small axial temperature difference for each part within the core length. Meanwhile, due to the good heat dissipation capacity of the windings in the core, the temperature of the end windings is higher than that of the windings in the core. Comparison of Table 8 with Table 6 shows that the CS-PMSM can run safely when water cooling used in the casing and in the inner rotor are simultaneously adopted in the CS-PMSM. Comparison of Table 8 with Table 7 shows that the temperature of each part when the axial force air is used in the machine is lower than the temperature of each part when the water cooling is used in the inner rotor. This is mainly because the axial forced air can cool not only the inner rotor core by the axial cooling slots and the air gap but also the end range. In contrast, the water cooling mode used in the inner rotor can only take away the heat of the inner rotor by the axial cooling slots.

5. Thermal Field Analysis under Low Speed and Rated Load Condition

5.1. Only Water Cooling Used in the Casing

When both the SM and the DRM are running at the low speed and rated load, the 3-D thermal field distribution is calculated under condition of only water cooling used in the casing, as shown in Figure 17.

Figure 17. Thermal field distribution under condition of only water cooling used in the casing when both the SM and the DRM are running at the low speed and rated load.

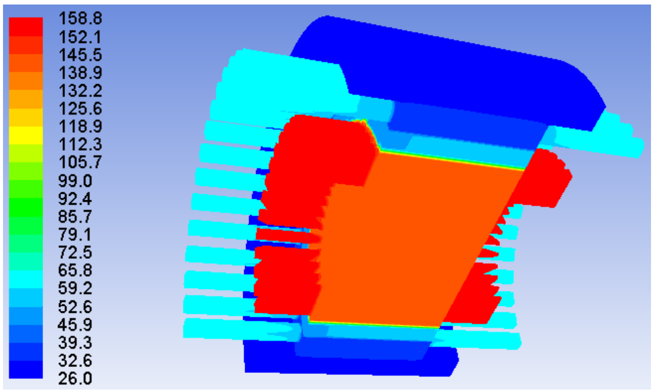

To illustrate the axial thermal field distribution of the CS-PMSM, the thermal field distributions of the water inlet side, middle cross-section, and the water outlet side of the CS-PMSM are shown in Figure 18. The selected water inlet, middle and water outlet cross-sections are the same as those in Section 4.1.

Figure 18. Thermal field distribution of three cross-sections: (**a**) the water inlet side; (**b**) the middle cross-section; and (**c**) the water outlet side.

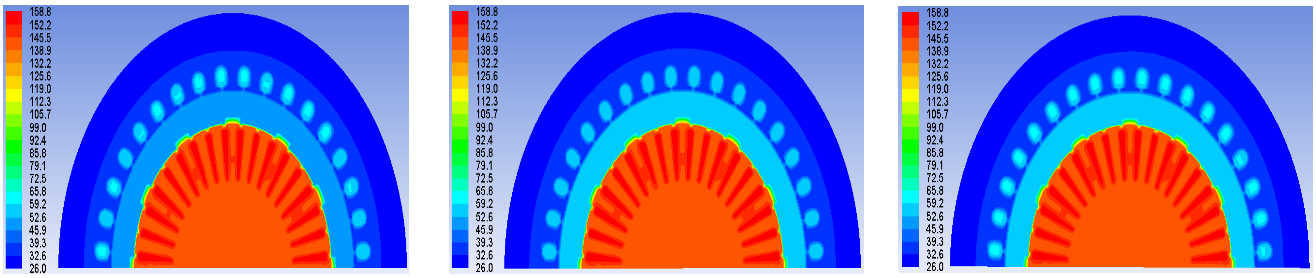

(**a**) (**b**) (**c**)

The highest temperature of different parts in the above three cross-sections is shown in Table 9. Meanwhile, the temperatures of the end windings of the stator and inner rotor are also listed in Table 9. From the temperature distribution of each cross-section in Table 9, it can be seen that the stator temperature is much lower than the temperature of the inner rotor, indicating that the water cooling used in the casing has a good cooling effect on the stator, but it has a poor cooling effect on the inner rotor. Besides, the temperature of inner rotor has reached 158.8 °C, higher than the temperature limitation of the class F insulation. By comparison of the temperature of the same part in three cross-sections, it shows that there is a small axial temperature difference for each part within the core length. Since the heat dissipation capacity of stator end windings are poorer than that of the windings in the core, the temperature of the stator end windings is higher than that of the windings in the core. However, the heat dissipation capacity of inner rotor windings in the core is poor for the inner rotor windings, so the temperature of inner rotor windings in the core is higher than that of end windings. Comparing Table 9 with Table 6, it shows that the temperature of each part under condition of the low speed and rated load is much lower than that under condition of the rated speed and rated load.

Table 9. Highest temperatures of different parts in the CS-PMSM.

Regions	**Highest temperature (°C)**		
	Water inlet side	**Middle**	**Water outlet side**
Inner rotor end windings	157	-	157.1
Inner rotor windings in the inner rotor core	157.7	158.8	157.7
Inner rotor core	145.3	145.7	145
Inner PMs	51.6	55.6	54.7
Outer rotor core	51.3	55	54.2
Outer PMs	51	54.7	53.8
Stator core	37.5	40	41.5
Stator windings in the stator core	59.4	58.5	59.5
Stator end windings	64.1	-	64.5

5.2. Water Cooling Used in the Casing and Axial Forced Air

When both the SM and the DRM are running at the low speed and rated load, the 3-D thermal-field distribution is calculated under condition of water cooling used in the casing and axial forced air, as shown in Figure 19.

Figure 19. Thermal field distribution under condition of water cooling used in the casing and axial forced air when both the SM and the DRM run at the low speed and rated load.

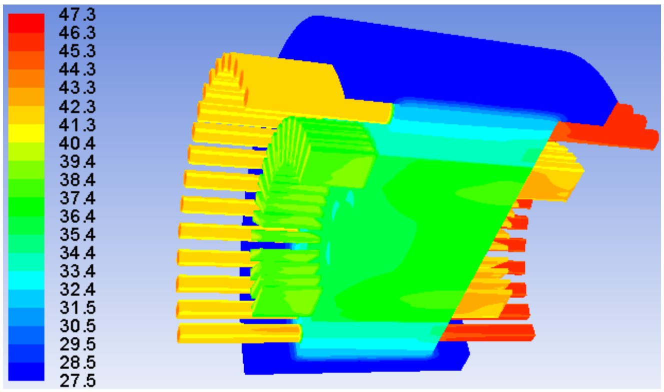

To illustrate the axial thermal field distribution of the CS-PMSM, the thermal field distributions of the windward side, middle cross-section, and the leeward side of the CS-PMSM are shown in Figure 20. The selected windward and leeward cross-sections are the same as those in Section 4.2.

Figure 20. Thermal field distribution of three cross-sections: (**a**) the windward side; (**b**) the middle cross-section; and (**c**) the leeward side.

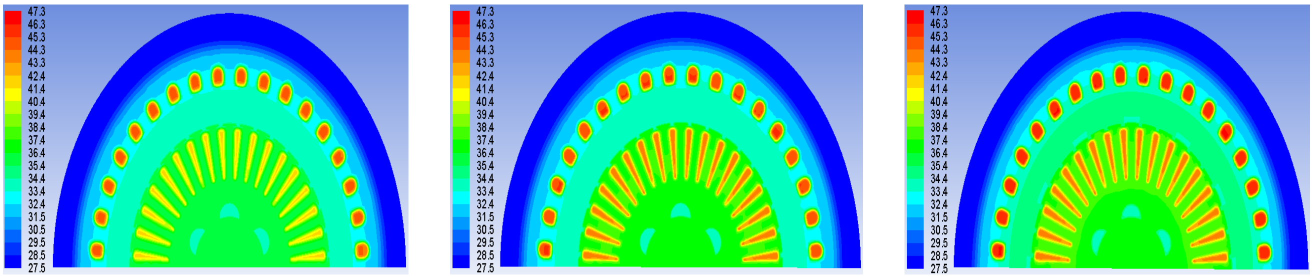

(**a**) (**b**) (**c**)

The highest temperature of different parts in the above three cross-sections is shown in Tables 10. Meanwhile, the temperatures of the end windings of the stator and inner rotor are also listed in Table 10.

Table 10. Highest temperatures of different parts in the CS-PMSM.

Regions	**Highest temperature (°C)**		
	Windward side	**Middle**	**Leeward side**
Inner rotor end windings	39.9	-	43.5
Inner rotor windings in the inner rotor core	41.7	43.3	43.3
Inner rotor core	36.4	37.8	37.9
Inner PMs	34.1	34.3	34.6
Outer rotor core	34.1	34.2	34.6
Outer PMs	34.1	34.2	34.6
Stator core	33.6	33.8	34.1
Stator windings in the stator core	44.5	45.4	46.4
Stator end windings	43.7	-	47.2

From the temperature distribution of each cross-section in Table 10, it can be seen that the temperatures of the stator and inner rotor are very low, indicating that the axial force air has a good cooling effect on the CS-PMSM, especially for the inner rotor. Meanwhile, due to the use of axial forced air, the temperature of the end windings at the windward side is much lower than that at the leeward side. By comparison of Tables 10 and 9, it shows that the CS-PMSM can run safely when the water cooling used in the casing and axial forced air are simultaneously adopted in the CS-PMSM.

5.3. Water Cooling Used in the Casing and the Inner Rotor

When both the SM and the DRM are running at the low speed and rated load, the 3-D thermal field distribution is calculated under condition of water cooling used in the casing and the inner rotor, as shown in Figure 21.

To illustrate the axial thermal field distribution of the CS-PMSM, the thermal field distributions of the water inlet side, middle cross-section, and the water outlet side of the CS-PMSM are shown in Figure 22. The selected water inlet, middle and water outlet cross-sections are the same as those in Section 4.1.

Figure 21. Thermal field distribution under condition of water cooling used in the casing and the inner rotor when both the SM and the DRM run at the low speed and rated load.

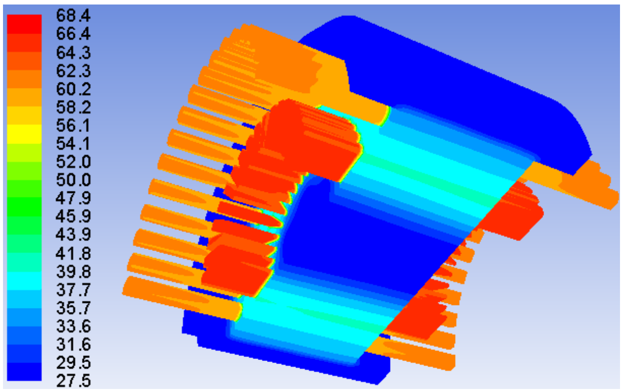

Figure 22. Thermal field distribution of three cross-sections: (**a**) the water inlet side; (**b**) the middle cross-section; and (**c**) the water outlet side.

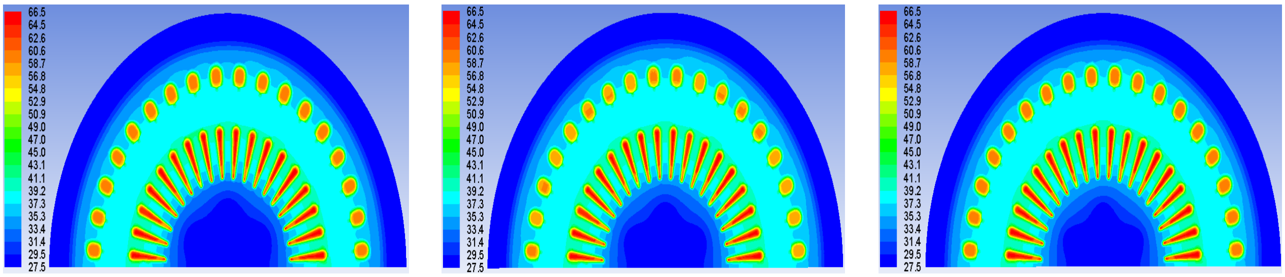

(**a**) (**b**) (**c**)

The highest temperature of each part in the above three cross-sections is shown in Table 11. Meanwhile, the temperatures of the end windings of the stator and inner rotor are also listed in Table 11. From the temperature distribution of each cross-section in Table 11, it can be seen that the temperatures of the stator windings and inner rotor windings are higher than others. This is mainly because the windings are the major heat source under condition of the low speed and rated load. By comparison of the temperature of the same part in three cross-sections, it shows that there is a small axial temperature difference for each part within the core length. Meanwhile, due to the good heat dissipation capacity of the windings in the core, the temperature of the end windings is higher than that of the windings in the core. Comparing Table 11 with Table 9, it shows that the CS-PMSM can run safely when the water cooling used in the casing and water cooling used in the inner rotor are simultaneously adopted in the CS-PMSM. Comparing Tables 11 with Table 10, it shows that the temperature of each part when the axial force air is used in the machine is lower than the temperature of each part when the water cooling is used in the inner rotor. This is mainly because the axial forced air can cool not only the inner rotor core by the axial cooling slots and the air gap but also the end range. In contrast, the water cooling mode used in the inner rotor can only take away the heat of the inner rotor by the axial cooling slots.

Table 11. Highest temperature of different parts in the CS-PMSM.

Regions	**Highest temperature (°C)**		
	Water inlet side	**Middle**	**Water outlet side**
Inner rotor end windings	68.1	-	68.4
Inner rotor windings in the inner rotor core	66.2	66.4	66.6
Inner rotor core	41.2	41.2	41.3
Inner PMs	38.2	38.3	38.3
Outer rotor core	38.2	38.3	38.3
Outer PMs	38.2	38.3	38.3
Stator core	38.5	37.6	38.4
Stator windings in the stator core	59.8	59	60
Stator end windings	61.7	-	62.1

6. Multi-Point Temperature Measuring System for the CS-PMSM

Considering the complexity of the high efficiency cooling system, a real-time multi-point temperature measuring system for the CS-PMSM is investigated in this section. Since there is limited room left in the shaft for the lead wire, the two-wire thermal sensors (PT100) are employed to acquire thermal data. On one hand, the resistances of the sensors' wires and the precision of circuit components will affect the test results. On the other hand, the intensive EMI during the operation of the machine causes disturbance to the output voltage of the sensor. Therefore, the digital linear calibration and filter are used to solve the above problems in this paper.

6.1. Linear Measurement and Calibration

In reference [51], in order to calibrate the linear error of A/D converter, two voltage references are used as input to detect the gain and offset error. If a linear circuit as shown in Figure 23 is used for resistance-voltage conversion, the conversion function can be expressed by:

$$U_0 = \left[0.15\left(1+\frac{R_5}{R_3}\right)-\frac{5R_5R_{\mathrm{w}}}{R_1R_3}\right]\left(1+\frac{R_7}{R_6}\right)-\frac{5R_5}{R_1R_3}\left(1+\frac{R_7}{R_6}\right)R_{\mathrm{t}} \tag{12}$$

where U_0 is the output voltage; R_{w} is the lead resistance; and R_{t} is the input resistance.

Figure 23. Schematic circuit for resistance-to-voltage conversion.

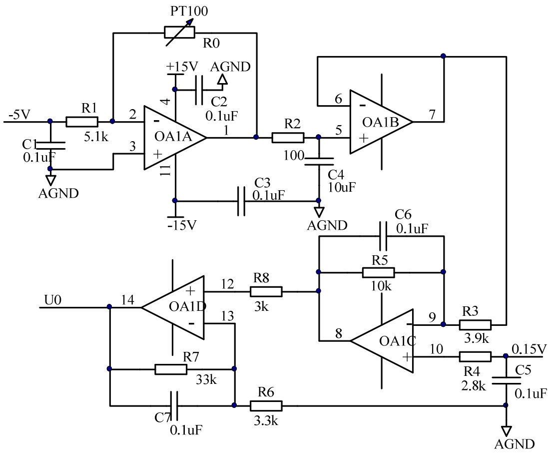

By defining:

$$a = -\frac{5R_5}{R_1R_3}\left(1+\frac{R_7}{R_6}\right) \tag{13}$$

$$b = \left[0.15\left(1+\frac{R_5}{R_3}\right)-\frac{5R_5R_w}{R_1R_3}\right]\left(1+\frac{R_7}{R_6}\right) \tag{14}$$

Equation (12) can be expressed as:

$$U_0 = aR_t + b \tag{15}$$

where a is the ideal gain; and b is the ideal offset.

Hence, the gain and offset of the circuit can be calculated with two reference resistors and their output voltages at each circuit warm-up. In this way, the measuring error introduced by the lead resistance and component precision could be eliminated. The actual gain and offset of the conversion circuit can be calculated as described earlier:

$$a' = \frac{U_1 - U_2}{R_1 - R_2} \tag{16}$$

$$b' = U_1 - R_1\frac{U_1 - U_2}{R_1 - R_2} \tag{17}$$

where a' and b' are the actual gain and offset; R_1 and R_2 are two different input resistors; U_1 and U_2 are their corresponding output voltages. For the given resistor R_3 and output voltage U_3, the actual resistance ought to be:

$$R'_3 = \frac{U_3 - b'}{a'} \tag{18}$$

6.2. Principle of EMI Suppression

During the operation of the CS-PMSM, the intensive alternating electromagnetic field leads to output voltage disturbances, which consist of the synchronous and harmonic components produced by the magnetic field. Owing to the hardware low-pass filter, the high-frequency interference component such as modulation and switching frequencies and their harmonics are attenuated to a negligible degree. However, when the CS-PMSM operates at low speed, the low-frequency interference signals cannot be eliminated by the hardware low-pass filter. Thus, digital filtering is employed to deal with interferences merging in the sample data. Since the thermal signal changes slowly, it is approximately direct current (DC) if the sample window is short enough, therefore, the DC component of the sample data can be extracted as the actual thermal data. However, an interference leakage on DC component is caused by the asynchronous sampling, since the speed of motor is varying. To solve this problem, a four-term Blackman-Harris sampling window is applied:

$$w(n) = a_0 - a_1\cos\left(\frac{2\pi n}{N\text{-}1}\right) + a_2\cos\left(\frac{4\pi n}{N\text{-}1}\right) - a_3\cos\left(\frac{6\pi n}{N\text{-}1}\right) \tag{19}$$

where $a_0 = 0.35875$; $a_1 = 0.48829$; $a_2 = 0.14128$; $a_3 = 0.01168$; and N is the sampling length.

Compared to a rectangular window, the four-term Blackman-Harris window has a prominent low-pass feature in the attenuation of interference leakage on DC component, as shown in Figure 24.

Figure 24. Attenuation of interference leakage on direct current (DC) component by different windows: (**a**) rectangle window; and (**b**) four-term Blackman-Harris window.

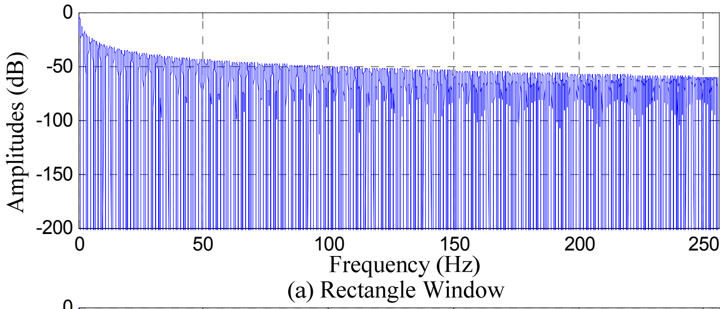

(a) Rectangle Window

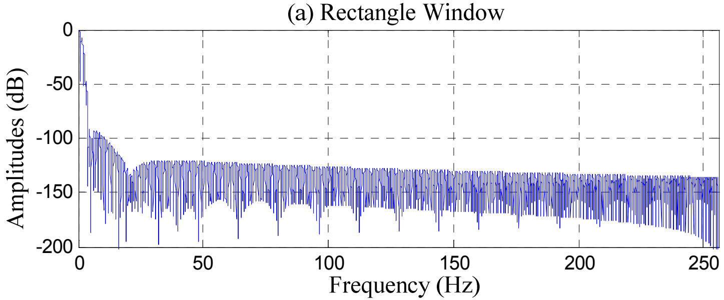

(b) 4-term Blackman-Harris window

Assume that the length of the sampling sequence $\{x(n)\}$ is N. The sampling frequency satisfies the Shannon theorem. By making use of the 4-term Blackman-Harris window method, the DC component can be expressed as:

$$X_{\mathrm{w}}(0) = \frac{1}{N \cdot G}\sum_{n=0}^{N-1} x(n) w_{\mathrm{b}}(n) \tag{20}$$

where $G = 0.36$ is the gain of the window; and $w_{\mathrm{b}}(n)$ is window coefficient.

6.3. Test Results

The sampling rate and data length determines the frequency bandwidth and resolution in FFT. Considering the maximum interference frequency, during the experiment, each sensor was sampled at 512 Hz with the data length of 512. Hence, the maximum transformed frequency is 256 Hz with 1 Hz resolution. Based on the resistance-to-voltage circuit in Figure 23, the output analog signals were further converted to digital signals by a 16-bit analogy-to-digital converter controlled by an MCU LPC 2294. Since the overall data amount exceeded the processing capability of the MCU, the sample data were sent to a PC via CAN bus. The digital filtering, linear calibration, calculation, real-time data display and storage are realized by the PC software. By a precision resistance meter, the measuring errors before and after linear calibration were compared without EMI, as shown in Figure 25. It is observed that the linear calibration has reduced the measuring error dramatically.

For simplicity, the thermal data are sampled when the SM is operating under rated load and the DRM is operating at no load. In this case, the inner rotor is locked and the outer rotor is at rated speed. The running machine was supplied by a KEB inverter that employs $i_{\mathrm{d}} = 0$ field-oriented control strategy with SVPWM modulation. The original temperature signal and its spectrum are shown in Figures 26 and 27, respectively. It is found that the temperature signal is severely interfered by EMI even filtered by hardware low-pass filter. The spectrum shows that the synchronous component (5.5 Hz) along with the harmonic components is the main factor of the interferences. When both the SM and DRM are operating, the spectrum of the sampling data should contain the synchronous and harmonics components produced by the two machines.

Figure 25. Effect of linear error calibration.

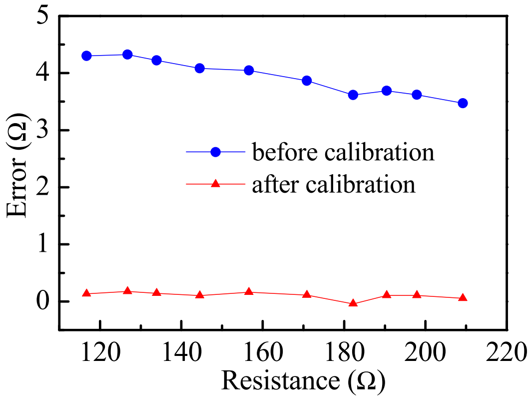

Figure 26. Effect of linear error calibration.

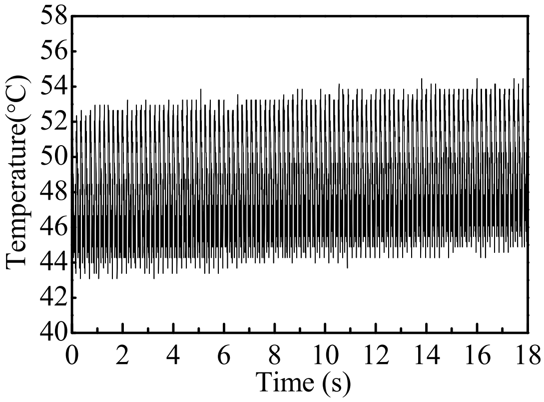

Figure 27. Frequency spectrum of original temperature signal.

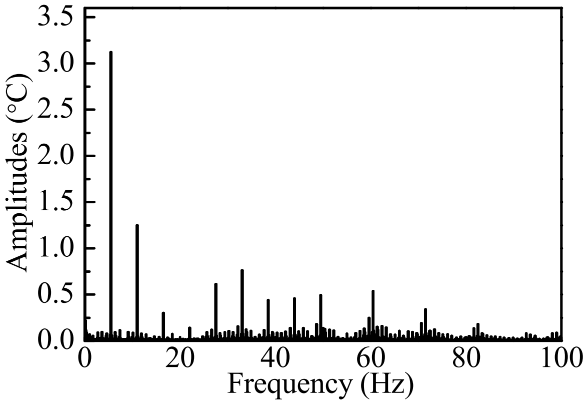

The actual temperature signals obtained through both rectangle and four-term Blackman-Harris windowed method are shown in Figure 28. It can be seen that a better suppression of inference leakage and smoother waveform are achieved with the proposed four-term Blackman-Harris windowed average method.

Figure 28. Temperature signals filtered by rectangle and four-term Blackman-Harris windowed average method.

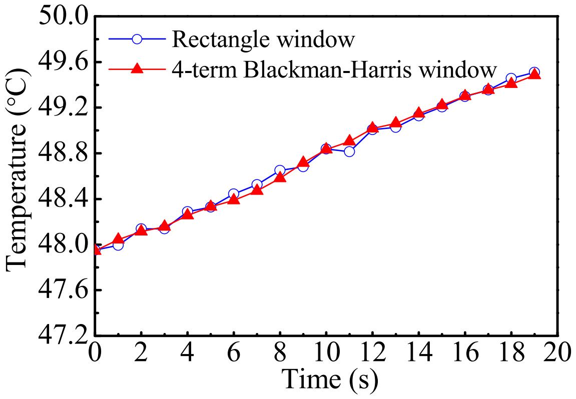

The above experimental results indicate that the linear calibration can eliminate the error caused by the lead wire and component precision of the circuit. The four-term Blackman-Harris windowed average method can suppress the EMI produced by the operating machine. An accurate and anti-interference multi-point temperature measuring system for the CS-PMSM is realized, providing effective thermal feedback for the cooling system of CS-PMSM.

7. Experiments

7.1. The CS-PMSM Prototype

A prototype of the CS-PMSM is designed and its specific parameters are listed in Table 12. In the design, both SM and DRM apply the skewed slots with a skewing angle of 10° to diminish cogging torque and torque ripple. Multiple temperature sensors of PT100 are embedded in the windings of the SM and the DRM to measure the real-time temperature of key points in the machine.

Table 12. Specifications of the prototype.

Machine name	Rated power	Rated torque	Constant torque range	Constant power range	Base speed	Max speed
SM	10 kW	32 Nm	0–3000 rpm	3000–6000 rpm	3000 rpm	6000 rpm
DRM	10 kW	32 Nm	0–3000 rpm	-	-	3000 rpm

The main components of the CS-PMSM prototype are shown in Figure 29.

Figure 29. Main components of the CS-PMSM prototype: (**a**) inner rotor; (**b**) outer rotor; and (**c**) stator.


(**a**) (**b**) (**c**)

7.2. Temperature Rise Experiment of the CS-PMSM

To measure the temperature of the inner rotor windings, the inner rotor is locked in the testing process. Since the outer rotor is the common rotor of the SM and DRM, both machines are regarded as the load motor of each other. In this case, both machines can simultaneously run at the rated speed and rated torque, or run at the low speed and rated torque. In the test, the cooled water flows through the water channels in the casing and the forced air blows from one side of the machine by a fan. Besides, the measured ambient temperature is 21 °C.

Multiple temperature sensors of PT100 are embedded in end windings and the windings in the core for the SM and DRM. Meanwhile, to measure the temperature of the stator and inner rotor core, some temperature sensors of PT100 are attached to the inner wall of the slot. All the sensors are connected to the real-time multi-point temperature measuring system we have made according to the method in Section 6. Finally, the real-time temperature can be read from the above temperature measuring system.

Under the rated speed and rated torque working condition, The SM torque is set to 32 Nm by torque control, which equals the SM rated torque. Meanwhile, The DRM speed is set to the rated speed of 3000 rpm by speed control. In this case, both the SM and the DRM run under rated torque and rated speed conditions. Then two experiments are done under these working conditions.

In the first experiment, only water cooling is used in the casing, and the time-varying temperature of different parts in the SM and DRM is shown in Figure 30.

Figure 30. Experimental results when the SM and DRM run at rated torque and rated speed, and only water cooling is used in the casing: (**a**) the SM; and (**b**) the DRM.

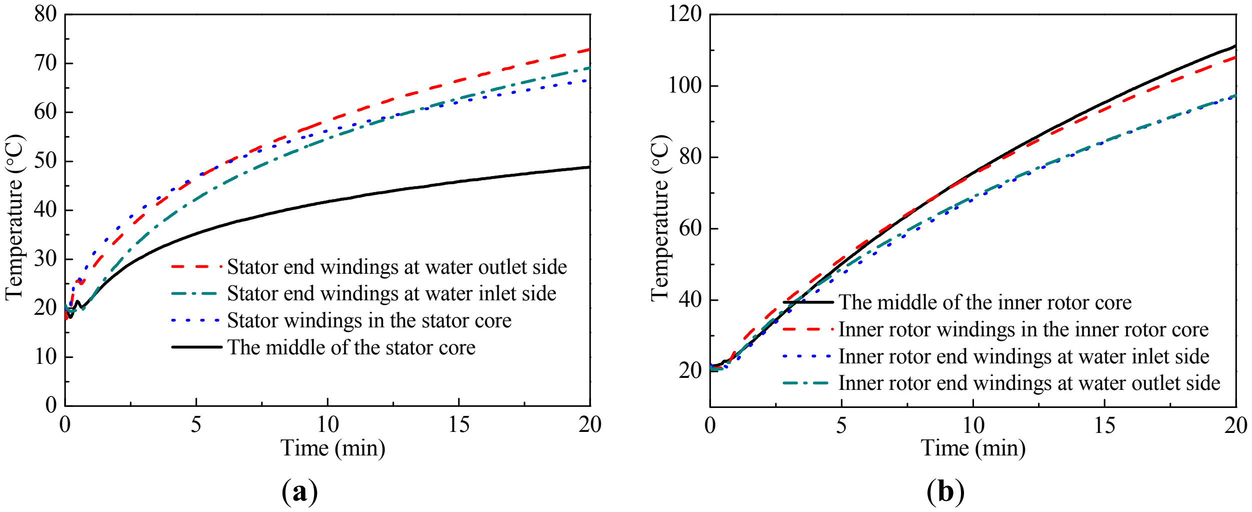

(**a**) (**b**)

Since the temperature increases very quickly, to ensure safety the experiment lasts for only 20 min and the measured temperature at 20 min is shown in Table 13. Based on the existing experimental data, the exponential function fitting method is used to obtain the steady tested temperature, for the transient temperature rise in electrical machines presents a rule of exponential function according to the heat transfer theory of the machine. Under the same conditions, the steady temperature calculated by FEM is also listed in Table 13. It can be seen that the steady temperature calculated by FEM is in good agreement with the tested steady temperature, which verifies the validity of the 3-D thermal-field model and analysis. It is clearly shown that the temperatures of different parts in the stator are much lower than those in the inner rotor. This indicates that the water cooling used in the casing has a good cooling effect on the stator, but it has a poor cooling effect on the inner rotor. Besides, the maximum temperature of inner rotor has reached 260.5 °C, obviously higher than the temperature limitation of the class F insulation.

Table 13. Calculated and tested temperatures in the prototype when the SM and DRM run at rated torque and rated speed, and only water cooling is used in the casing. FEM: finite-element method.

Regions	Tested temperature at 20 min (°C)	Inferred steady temperature from tested results (°C)	Calculated steady temperature by FEM (°C)
Stator end windings at water inlet side	69.1	107.6	103.6
Stator end windings at water outlet side	72.9	109.5	104.7
Stator windings in the stator core	66.6	104.7	101.2
The middle of the stator core	48.8	92.7	88.4
Inner rotor end windings at water inlet side	97.1	247.3	241.4
Inner rotor end windings at water outlet side	97.4	247.9	241.4
Inner rotor windings in the inner rotor core	108.1	255	247.2
The middle of the inner rotor core	111.3	260.5	247

In the second experiment, water cooling is used in the casing; and the forced air blows along axial direction by a powerful fan. The time-varying temperature of different parts in the SM and DRM is shown in Figure 31.

Figure 31. Experimental results when the SM and DRM run at rated torque and rated speed, and water cooling and forced air are used in the machine: (**a**) the SM; and (**b**) the DRM.

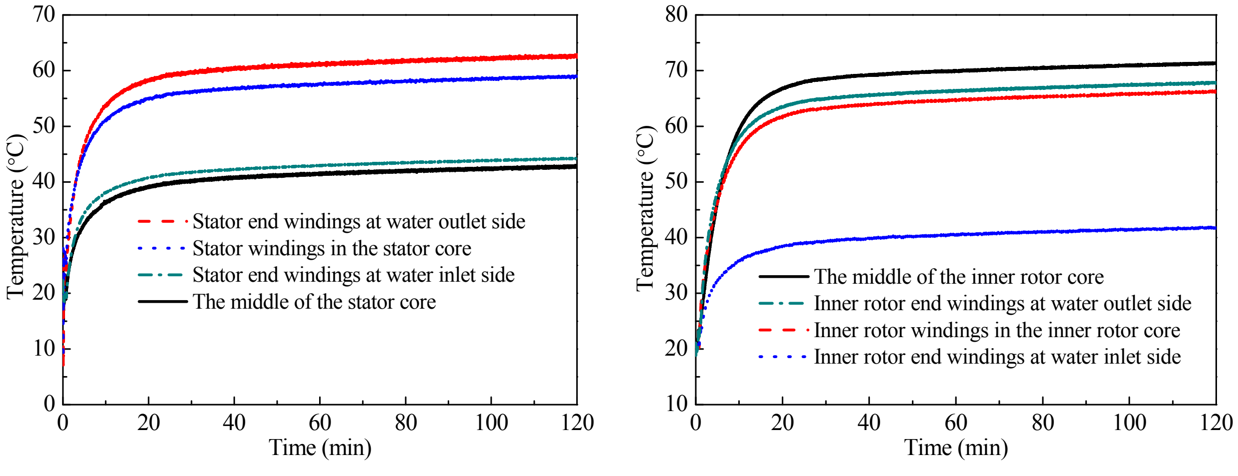

(**a**) (**b**)

The steady temperature measured and calculated by FEM is shown in Table 14. It is clearly shown that the maximum temperature of inner rotor is 71.3 °C, much lower than the temperature limitation of the class F insulation. So the motor can run safely. Comparing Table 13 with Table 14, it is clearly shown that the inner rotor temperature decreases significantly when axial direction forced air exists. At the same time, the stator temperature also decreases to some extent. It shows that forced air has great cooling effect on the motor, especially on the inner rotor. Therefore, the CS-PMSM can run safely under the rated torque and rated speed working conditions only if both water cooling and forced air exist.

Table 14. Calculated and tested temperatures in the prototype when the SM and DRM run at rated torque and rated speed, and water cooling and force air are used in the machine.

Regions	Calculated highest steady temperature (°C)	Tested highest steady temperature (°C)
Stator end windings at water inlet side	48.3	44.2
Stator end windings at water outlet side	58.9	62.4
Stator windings in the stator core	54	58.9
The middle of the stator core	45	42.7
Inner rotor end windings at water inlet side	50.1	41.7
Inner rotor end windings at water outlet side	62.8	67.8
Inner rotor windings in the inner rotor core	63.1	66.2
The middle of the inner rotor core	86.8	71.3

Under the low speed and rated torque working condition, The SM's torque is set to 32 Nm by torque control, which equals the SM's rated torque. Meanwhile, The DRM's speed is set to the speed of 200 rpm by speed control. In this case, both the SM and the DRM run under rated torque and low speed condition. Then two experiments are done under this working condition.

In the first experiment, only water cooling is used in the casing, and the time-varying temperature of different parts in the SM and DRM is shown in Figure 32.

Figure 32. Experimental results when the SM and DRM run at rated torque and low speed, and only water cooling is used in the casing: (**a**) the SM; and (**b**) the DRM.

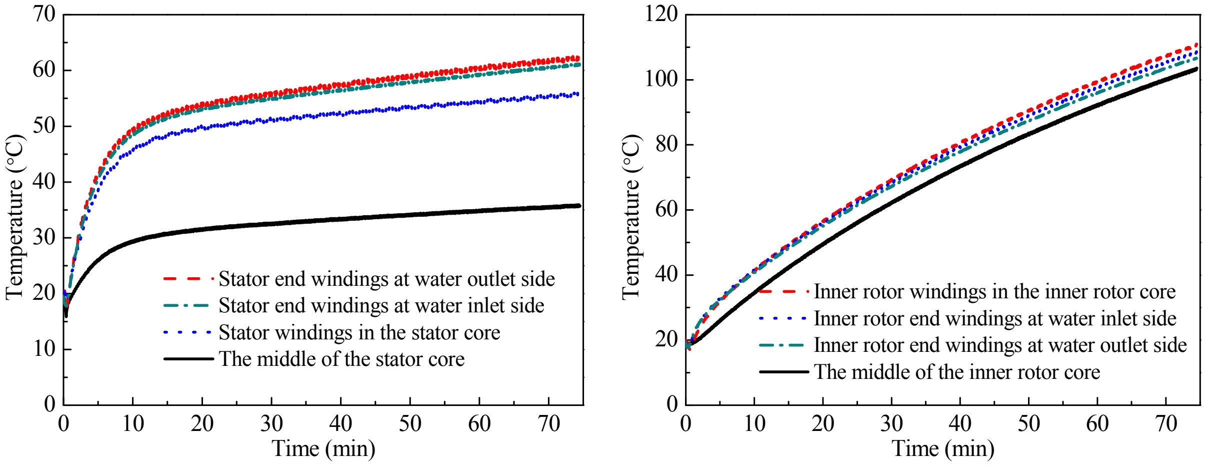

(**a**) (**b**)

To ensure safety, the experiment lasts for 75 min and the measured temperature at 75 min is shown in Table 15. We can see that the temperature of the stator is basically in a steady state, but the temperature of the inner rotor is still not reaching a steady state. Therefore, the exponential function fitting method is used to obtain the steady tested temperature based on the existing experimental data. Under the same condition, the steady temperature calculated by FEM is also listed in Table 15. It can be seen that the steady temperature calculated by FEM is in good agreement with the steady tested temperature, which verifies the validity of the 3-D thermal-field model and analysis. It is clearly shown that the temperature of each part in the stator is much lower than the temperature of each part in the inner rotor. This indicates that the water cooling used in the casing has a good cooling effect on the stator, but it has a poor cooling effect on the inner rotor. Besides, the maximum temperature of inner rotor has reached 169.5 °C, obviously higher than the temperature limitation of the class F insulation.

Table 15. Calculated and tested highest temperatures in the prototype when the SM and DRM run at rated torque and low speed, and only water cooling is used in the casing.

Regions	Tested temperature at 75 min (°C)	Inferred steady temperature from tested results (°C)	Calculated steady temperature by FEM (°C)
Stator end windings at water inlet side	61.2	70.7	64.1
Stator end windings at water outlet side	62.2	71.4	64.5
Stator windings in the stator core	55.8	62.3	58.5
The middle of the stator core	35.7	45.1	40
Inner rotor end windings at water inlet side	108.5	163.4	157
Inner rotor end windings at water outlet side	106.6	160.4	157.1
Inner rotor windings in the inner rotor core	110.9	169.5	158.8
The middle of the inner rotor core	103.6	154.3	145.7

In the second experiment, water cooling is used in the casing; and the forced air is blown along the axial direction by a powerful fan. The time-varying temperature of different parts in the SM and DRM is shown in Figure 33.

The steady temperature measured and calculated by FEM is shown in Table 16. It is clearly shown that the maximum temperature of the stator and the inner rotor are 47.1 °C and 42.6 °C, respectively, much lower than the temperature limitation of the class F insulation. Therefore, the motor can run safely. Comparing Table 15 with Table 16, it is clearly shown that the inner rotor temperature decreases significantly when axial direction forced air exists. At the same time, the stator temperature also decreases to some extent. It shows that forced air has great cooling effect on the motor, especially on the inner rotor. Therefore, the CS-PMSM can run safely under the rated torque and low speed working condition only if both water cooling and forced air exist.

Figure 33. Experimental results when the SM and DRM run at rated torque and low speed, and water cooling and forced air are used in the machine: (**a**) the SM; and (**b**) the DRM.

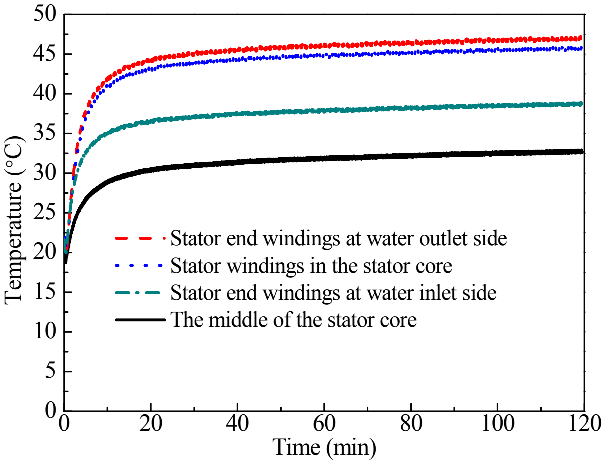

(**a**)

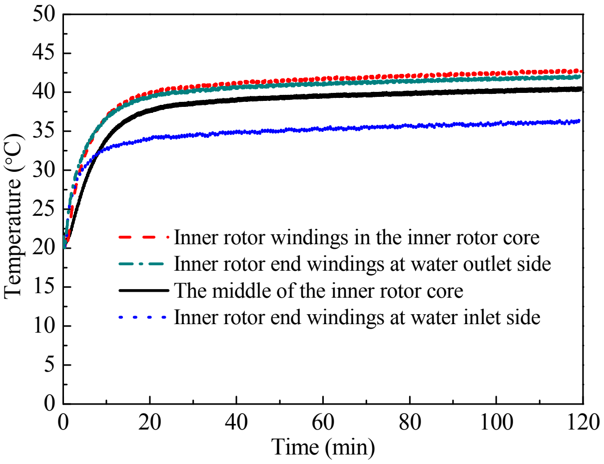

(**b**)

Table 16. Calculated and tested highest temperatures in the prototype when the SM and DRM run at rated torque and low speed, and water cooling and forced air are used in the machine.

Regions	Calculated highest steady temperature (°C)	Tested highest steady temperature (°C)
Stator end windings at water inlet side	43.7	38.9
Stator end windings at water outlet side	47.2	47.1
Stator windings in the stator core	45.4	46
The middle of the stator core	33.8	32.7
Inner rotor end windings at water inlet side	39.9	36.1
Inner rotor end windings at water outlet side	43.5	41.9
Inner rotor windings in the inner rotor core	43.3	42.6
The middle of the inner rotor core	37.8	40.6

8. Conclusions

(1) A coupling surface method is proposed for the random winding machine, which can compute the heat transfer effect in the end windings as well as that between end windings and the windings in the slots; and simplify 3-D thermal model of the end windings.

(2) To monitor the temperature of the CS-PMSM, a real-time multi-point temperature measuring system is built. By using the linear calibration and the four-term Blackman-Harris windowed average method in this system, the error caused by the lead wire and component precision of the circuit is eliminated and the EMI produced by the operating machine is suppressed.

(3) The comprehensive and accurate research has been done on the temperature rising problem of the CS-PMSM from the thermal-field distribution law to the temperature monitoring system. The influence law of the forced air and water cooling on the temperature rising of the CS-PMSM is obtained. The method that the CS-PMSM can obtain safe and reliable operation is proposed. It can provide a theoretical basis for the design of the cooling system.

(4) The simulation and experiment results show that when only water cooling is used in the casing, the CS-PMSM can't run safely under the conditions of rated speed and rated load or low speed and rated load, as the temperature of the inner rotor is much higher than the temperature limitation of the winding insulation. When water cooling is used in the casing and axial forced air exists in the machine, the CS-PMSM can run safely under the conditions of rated speed and rated load or low speed and rated load. Besides, by comparison of the simulation and experiment results under different conditions of the CS-PMSM, the validity of the 3-D thermal-field model and analysis is verified.

Acknowledgments

This work was supported in part by National Natural Science Foundation of China under Project 51077026, 51377030 and 51325701, in part by the 863 Plan of China under Project 2011AA11A261.

Conflicts of Interest

The authors declare no conflict of interest.

References

1. Dorrell, D.G.; Knight, A.M.; Evans, L.; Popescu, M. Analysis and design techniques applied to hybrid vehicle drive machines assessment of alternative IPM and induction motor topologies. *IEEE Trans. Ind. Electron.* **2012**, *59*, 3690–3699.
2. Zhang, X.W.; Li, C.T.; Kum, D.; Peng, H. $_{\text{Prius}}{}^{+}$ and $_{\text{Volt}}{}^{-}$: Configuration analysis of power-split hybrid vehicles with a single planetary gear. *IEEE Trans. Veh. Technol.* **2012**, *61*, 3544–3552.
3. Arakawa, T.; Takemoto, M.; Ogasawara, S.; Inoue, K.; Ozaki, O.; Hojo, H.; Mitani, H. Examination of an interior permanent magnet type axial gap motor for the hybrid electric vehicle. *IEEE Trans. Magn.* **2011**, *47*, 3602–3605.
4. Chau, K.T.; Chan, C.C. Emerging energy-efficient technologies for hybrid electric vehicles. *IEEE Proc.* **2007**, *95*, 821–835.
5. Ho, S.L.; Niu, S.X.; Fu, W.N. Transient analysis of a magnetic gear integrated brushless permanent magnet machine using circuit-field-motion coupled time-stepping finite element method. *IEEE Trans. Magn.* **2010**, *46*, 2074–2077.
6. Bertoluzzo, M.; Bolognesi, P.; Buja, G.; Thakura, P. Role and Technology of the Power Split Apparatus in Hybrid Electric Vehicles. In Proceedings of the 33rd Annual Conference of the IEEE Industrial Electronics Society (IECON), Taipei, Taiwan, 5–8 November 2007; Volume 5, pp. 256–261.
7. Syed, F.U.; Kuang, M.L.; Ying, H. Active damping wheel-torque control system to reduce driveline oscillations in a power-split hybrid electric vehicle. *IEEE Trans. Veh. Technol.* **2009**, *58*, 4769–4875.
8. Mashadi, B.; Emadi, S. Dual-mode power-split transmission for hybrid electric vehicles. *IEEE Trans. Veh. Technol.* **2010**, *59*, 4769–4875.

9. Cheng, Y.; Trigui, R.; Espanet, C.; Bouscayrol, A.; Cui, S. Specifications and design of a PM electric variable transmission for Toyota Prius II. *IEEE Trans. Veh. Technol.* **2011**, *60*, 4106–4114.
10. Liu, Y.; Tong, C.D.; Bai, J.G.; Yu, S.; Tong, W.M.; Fu, W.N. Optimization of an 80 kW radial-radial flux compound-structure permanent-magnet synchronous machine used for HEVs. *IEEE Trans. Magn.* **2011**, *47*, 2399–2402.
11. Zeng, X.H.; Zheng, S.; Song, D.F. Modeling and Dynamic Simulation of a Virtual Prototype for Applying Automobile Differential into Hybrid Electric Vehicle as Power-slit Device. In Proceedings of the International Conference on Computer Application and System Modeling (lCCASM), Taiyuan, Shanxi, China, 22–24 October 2010; pp. V3-82–V3-87.
12. Liu, J.M.; Peng, H. Modeling and control of a power-split hybrid vehicle. *IEEE Trans. Control Syst. Technol.* **2008**, *16*, 1242–1251.
13. Zheng, P.; Liu, R.R.; Shen, L.; Li, L.; Fan, W.; Wu, Q.; Zhao, J. Evaluation of performance and magnetic characteristics of a radial-radial flux compound-structure permanent-magnet synchronous machine used for hybrid electric vehicle. *J. Appl. Phys.* **2008**, *103*, 07F130:1–07F130:3, doi:10.1063/1.2839776.
14. Zheng, P.; Zhao, J.; Wu, Q.; Fan, W.; Shen, L.; Li, L.; Liu, R. Evaluation of the magnetic coupling degree and performance of an axial-axial flux compound-structure permanent-magnet synchronous machine used for hybrid electric vehicles. *J. Appl. Phys.* **2008**, *103*, 07F113:1–07F113:3, doi:10.1063/1.2834398.
15. Eriksson, S.; Sadarangani, C. A Four-Quadrant HEV Drive System. In Proceedings of the IEEE 56th Vehicular Technology Conference, Vancouver, BC, Canada, 24–28 September 2002; Volume 3, pp. 1510–1514.
16. Hoeijmakers, M.J.; Rondel, M. The Electrical Variable Transmission in a City Bus. In Proceedings of the IEEE 35th Annual Power Electronics Specialists Conference (PESC), Aachen, Germany, 20–25 June 2004; Volume 4, pp. 2773–2778.
17. Xu, L.Y. A New Breed of Electrical Machines-Basic Analysis and Applications of Dual Mechanical Port Electric Machines. In Proceedings of the 8th International Conference on Electric Machines and Systems, Nanjing, Jiangsu, China, 27–29 September 2005; Volume 1, pp. 24–31.
18. Guo, X.Z.; Wen, X.H.; Xu, L.Y.; Zhao, F.; Liu, J. Vibration Reducing in the Process of Engine Start-stop for Electric Variable Transmission. In Proceedings of the IEEE 6th International Power Electronics and Motion Control (IPEMC) Conference, Wuhan, Hubei, China, 17–20 May 2009; pp. 2001–2004.
19. Liu, Y.; Cheng, D.S.; Sui, Y.; Bai, J.; Tong, C.; Tong, W. Magnetic system study of a compound-structure permanent-magnet synchronous machine for HEVs. *IEEE Trans. Ind. Appl.* **2012**, *48*, 1797–1807.
20. Song, X.L.; Wen, X.H.; Zhao, F.; Liu, J.; Xu, L. A Control and Drive System for Permanent Magnetic Dual Mechanical Port Electric Machine Used in Hybrid Electric Vehicles. In Proceedings of the International Conference on Electrical Machines and Systems (ICEMS), Tokyo, Japan, 15–18 November 2009; pp. 1–4.
21. Xu, L.Y.; Zhang, Y.; Wen, X. Multioperational modes and control strategies of dual-mechanical-port machine for hybrid electrical vehicles. *IEEE Trans. Ind. Appl.* **2009**, *45*, 747–755.

22. Zhuang, X.M.; Wen, X.H.; Zhao, F.; Fan, T.; Wang, Y.X. A Control Strategy of Unified Field Permanent Magnet Dual Mechanical Port Machine with Spoke Type PM Arrangement. In Proceedings of the IEEE Vehicle Power and Propulsion Conference (VPPC), Seoul, Korea, 9–12 October 2012; pp. 83–87.
23. Abdelsalam, A.A.; Cui, S.M. Fuzzy Logic Global Power Management Strategy for HEV Based on Permanent Magnet-Dual Mechanical Port Machine. In Proceedings of the IEEE 7th International Power Electronics and Motion Control (IPEMC) Conference, Harbin, Heilongjiang, China, 2–5 June 2012; pp. 859–866.
24. Sun, X.K.; Cheng, M.; Zhu, S.; Zhang, J.Z. Coupled electromagnetic-thermal-mechanical analysis for accurate prediction of dual-mechanical-port machine performance. *IEEE Trans. Ind. Appl.* **2012**, *48*, 2240–2248.
25. Zhao, F.; Wen, X.H.; Chen, J.W. Modeling of PM-PM Dual Mechanical Ports Electric Machines. In Proceedings of the 32nd Annual Conference on IEEE Industrial Electronics, Pairs, France, 6–10 November, 2006; pp. 1251–1256.
26. Zhao, F.; Wen, X.H.; Guo, X.Z.; Han, L.; Guo, X.H. Study of Field Coupling in Dual Mechanical Port Electrical Machines. In Proceedings of the International Conference on Electrical Machines and Systems (ICEMS), Seoul, Korea, 8–11 October 2007; pp. 1591–1595.
27. Zhang, Y.; Xu, L.Y. Application of Dual Mechanical Port Machine in Hybrid Electrical Vehicles. In Proceedings of the IEEE Vehicle Power and Propulsion Conference (VPPC), Windsor, UK, 6–8 September 2006; pp. 1–5.
28. Tong, C.D.; Zheng, P.; Zhao, J.; Wu, Q. Investigation of a Unified Controller of Compound Structure Permanent-Magnet Synchronous Machine for HEV Applications. In Proceedings of the 14th Biennial IEEE Conference on Electromagnetic Field Computation (CEFC), Chicago, IL, USA, 9–12 May 2010; p. 1.
29. Guo, X.H.; Wen, X.H.; Xu, L.Y.; Zhao, F.; Liu, J. Simulation and Experiment Analysis of Dynamic Process for an EVT Based on Dual Mechanical Port Electric Machine. In Proceedings of the IEEE 6th International Power Electronics and Motion Control (IPEMC) Conference, Wuhan, Hubei, China, 17–20 May 2009; pp. 2010–2014.
30. Zheng, P.; Liu, R.R.; Fan, W.G.; Han, J.Q.; Li, J.W.; Kou, B.Q. Research on the Control of a Radial-Radial Flux Compound-Structure Permanent-Magnet Synchronous Machine Used for HEVs. In Proceedings of the 14th Symposium on Electromagnetic Launch Technology, Victoria, BC, Canada, 10–13 June 2008; pp. 1–6.
31. Guo, X.H.; Wen, X.H.; Chen, J.W.; Zhao, F.; Guo, X.Z. Simulation of an Electrical Variable Transmission Based on Dual Mechanical Ports Electric Machine with Clutch. In Proceedings of the IEEE Vehicle Power and Propulsion Conference (VPPC), Harbin, Heilongjiang, China, 3–5 September 2008; pp. 1–5.
32. Zheng, P.; Tong, C.D.; Bai, J.; Sui, Y.; Song, Z.; Wu, F. Magnetic decoupling design and experimental validation of a radial-radial flux compound-structure permanent-magnet synchronous machine for HEVs. *Energies* **2012**, *5*, 4027–4039.

33. Liu, Y.; Tong, C.D.; Liu, R.R.; Zhao, J.; Bai, J.G.; Zheng, P. Comprehensive Research on Compound-Structure Permanent-Magnet Synchronous Machine System Used for HEVs. In Proceedings of the IEEE Energy Conversion Congress and Exposition (ECCE), Atlanta, GA, USA, 12–16 September 2010; pp. 1617–1622.
34. Liu, R.R.; Zhao, H.; Tong, C.D.; Chen, G.; Zheng, P.; Gu, G. Experimental evaluation of a radial-radial-flux compound-structure permanent-magnet synchronous machine used for HEVs. *IEEE Trans. Magn*. **2009**, *45*, 645–649.
35. Li, Q.; Fao, T.; Zhao, F.; Wen, X.H. Electromagnetic Coupling Analysis of Permanent Magnet Dual Mechanical Ports Machine. In Proceedings of the International Conference on Electric Information and Control Engineering (ICEICE), Wuhan, Hubei, China, 15–17 April 2011; pp. 5889–5892.
36. Zheng, P.; Liu, R.R.; Wu, Q.; Zhao, J.; Yao, Z.Y. Magnetic coupling analysis of four-quadrant transducer used for hybrid electric vehicles. *IEEE Trans. Magn.* **2007**, *43*, 2597–2599.
37. Zheng, P.; Zhao, J.; Liu, R.; Tong, C.; Wu, Q. Magnetic characteristics investigation of an axial-axial flux compound-structure PMSM used for HEVs. *IEEE Trans. Magn.* **2010**, *46*, 2191–2194.
38. Zheng, P.; Thelin, P.; Chen, A.; Nordlund, E. Influence of saturation and saliency on the inductance of a four-quadrant transducer prototype machine. *IEEE Trans. Magn.* **2006**, *42*, 1319–1322.
39. Zheng, P.; Nordlund, E.; Thelin, P.; Sadarangani, C. Investigation of the winding current distribution in a 4-quadrant-transducer prototype machine. *IEEE Trans. Magn.* **2005**, *41*, 1972–1975.
40. Liu, Y.; Cheng, D.S.; Bai, J.G.; Tong, C.D.; Song, Z.Y.; Tong, W.M. Topology comparison of compound-structure permanent-magnet synchronous machines. *IEEE Trans. Ind. Appl.* **2012**, *48*, 2217–2222.
41. Zheng, P.; Liu, R.R.; Thelin, P.; Nordlund, E.; Sadarangani, C. Research on the cooling system of a 4QT prototype machine used for HEV. *IEEE Trans. Energy Convers*. **2008**, *23*, 61–67.
42. Sun, X.K.; Cheng, M. Thermal analysis and cooling system design of dual mechanical port machine for wind power application. *IEEE Trans. Ind. Electron.* **2013**, *60*, 1724–1733.
43. Domeki, H.; Ishihara, Y.; Kaido, C.; Kawase, Y.; Kitamura, S.; Shimomura, T.; Takahashi, N.; Yamada, T.; Yamazaki, K. Investigation of benchmark model for estimating iron loss in rotating machine. *IEEE Trans. Magn.* **2004**, *40*, 794–797.
44. Boglietti, A.; Cavagnino, A.; Parvis, M.; Vallan, A. Evaluation of radiation thermal resistances in industrial motors. *IEEE Trans. Ind. Appl.* **2006**, *42*, 688–692.
45. Boglietti, A.; Cavagnino, A.; Staton, D. Determination of critical parameters in electrical machine thermal models. *IEEE Trans. Ind. Appl.* **2008**, *44*, 1150–1159.
46. Boglietti, A.; Cavagnino, A. Analysis of the endwinding cooling effects in TEFC induction motors. *IEEE Trans. Ind. Appl*. **2007**, *43*, 1214–1222.
47. Chauveau, E.; Zaim, E.H.; Trichet, D.; Fouladgar, J. A statistical approach of temperature calculation in electrical machines. *IEEE Trans. Magn.* **2000**, *36*, 1826–1829.
48. Xypteras, J.; Hatziathanassiou, V. Thermal analysis of an electrical machine taking into account the iron losses and the deep-bar effect. *IEEE Trans. Energy Convers*. **1999**, *14*, 996–1003.
49. Hatziathanassiou, V.; Xypteras, J.; Archontoulakis, G. Electricalthermal coupled calculation of an asynchronous machine. *Arch. Electrotech.* **1994**, *77*, 117–122.

50. Li, W.L.; Cao, J.C.; Zhang, X.C. Electrothermal analysis of induction motor with compound cage rotor used for PHEV. *IEEE Trans. Ind. Electron.* **2010**, *57*, 660–668.
51. Tessarolo, A. *Application report F2810, F2811, and F2812 ADC Calibration*; Texas Instruments: Dallas, TX, USA, 2004.